J. Fluid Mech. (2014), *vol.* 753, *pp.* 254–278. © Cambridge University Press 2014
doi:10.1017/jfm.2014.360

Steady streaming in a two-dimensional box model of a passive cochlea

Elisabeth Edom[1], **Dominik Obrist**[1,2,†] and **Leonhard Kleiser**[1]

[1]Institute of Fluid Dynamics, ETH Zurich, 8092 Zürich, Switzerland

[2]ARTORG Center for Biomedical Engineering Research, University of Bern, 3010 Bern, Switzerland

(Received 20 November 2013; revised 28 May 2014; accepted 20 June 2014;
first published online 22 July 2014)

Acoustic stimulation of the cochlea leads to a travelling wave in the cochlear fluids and on the basilar membrane (BM). It has long been suspected that this travelling wave leads to a steady streaming flow in the cochlea. Theoretical investigations suggested that the steady streaming might be of physiological relevance. Here, we present a quantitative study of the steady streaming in a computational model of a passive cochlea. The structure of the streaming flow is illustrated and the sources of streaming are closely investigated. We describe a source of streaming which has not been considered in the cochlea by previous authors. This source is also related to a steady axial displacement of the BM which leads to a local stretching of this compliant structure. We present theoretical predictions for the streaming intensity which account for these new phenomena. It is shown that these predictions compare well with our numerical results and that there may be steady streaming velocities of the order of millimetres per second. Our results indicate that steady streaming should be more relevant to low-frequency hearing because the strength of the streaming flow rapidly decreases for higher frequencies.

Key words: biological fluid dynamics, biomedical flows

1. Introduction

The cochlea is part of our hearing sense. It consists of three coiled chambers (scalae) which are filled with different lymphatic fluids, of several compliant membranes which separate the scalae, and of a large number of sensory hair cells (figure 1). Mechanically, the most relevant membrane is the basilar membrane (BM) which separates the cochlea in a fluid space above the BM (scala vestibuli and scala media) and a fluid space beneath the BM (scala tympani).

Acoustic signals enter the cochlea through vibrations of the stapes which is attached to the oval window of the cochlea. The cochlea transforms these vibrations to travelling waves in the cochlear fluids and on the BM. Local resonance phenomena yield a frequency discrimination along the principal axis of the cochlea. At the places of resonance (characteristic places) the mechanical wave motion deflects hair bundles of the inner and outer hair cells. Such a deflection opens gated ion channels and

---

† Email address for correspondence: dominik.obrist@artorg.unibe.ch

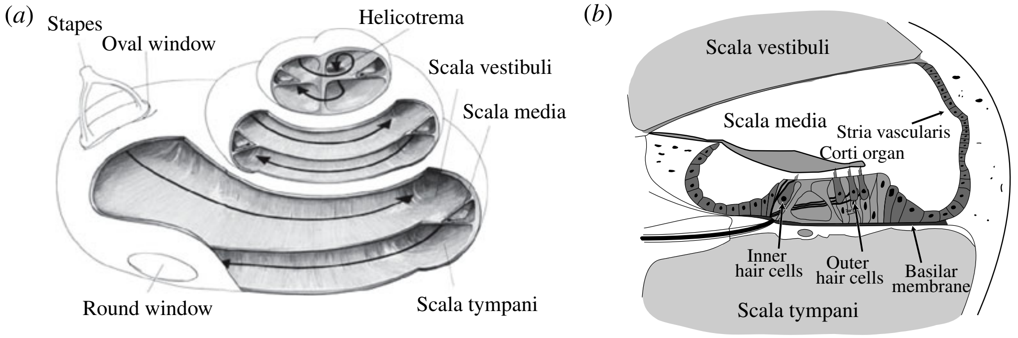

FIGURE 1. Schematics of (*a*) the cochlea with the three cochlear ducts (adapted from http://ptolentinobioresearch.wikispaces.com/) and (*b*) a cross-section through the scala media showing the BM and the Corti organ which includes the inner and outer hair cells (adapted from http://en.wikipedia.org/wiki/Cochlear_duct).

initializes a flux of K^+ ions into the hair cells. In interaction with further biochemical and neural processes, this leads to hearing. A comprehensive introduction into cochlear mechanics and modelling is given in Baker *et al.* (2006).

The term ‘steady streaming’ denotes a time-averaged fluid motion which is generated by an oscillating primary flow field with zero mean. Different types of steady streaming are known, e.g. the quartz wind which is induced by a high-intensity beam of sound, or the Rayleigh streaming induced by standing sound waves between plane walls. These streaming motions are nonlinear effects and forced by Reynolds stresses. In the present work, we also consider the Stokes drift as a steady streaming flow although its origin is of purely kinematic nature. Overviews of different streaming phenomena are given in, e.g., Lighthill (1978), Riley (2001), Boluriaan & Morris (2003) and Suh & Kang (2008).

Besides the streaming due to Reynolds stresses, we will find that the BM vibration is an additional source of cochlear streaming. In the general context of acoustic streaming, this mechanism was first pointed out by Bradley (1996). Applications of streaming due to vibrating walls have been discussed, for instance, by Luchini & Charru (2005) and Bradley (2012). In microfluidics the phenomenon is actively studied in the context of so-called ‘surface acoustic waves’ (Ding *et al.* 2013) which can be used for pumping in microfluidic devices (Vanneste & Bühler 2011) or for the manipulation of droplets (Tan *et al.* 2010).

In contrast to acoustic streaming phenomena which are directly related to acoustic waves, the steady streaming in the cochlea is caused by travelling waves in the cochlear fluids and on the BM. Although these waves run at acoustic frequencies, they are not acoustic waves. They are characterized by phase velocities of the order of 10 $m\ s^{-1}$ which is much lower than the typical acoustic wave speed, whereas the material velocities (of the order of millimetres per second) are much higher than in acoustic waves. They share some similarities with deep-water waves which are well known to lead to a Stokes drift (Andrews & McIntyre 1978). In contrast to deep-water waves, the cochlear waves feature thin Stokes boundary layers next to the BM where Reynolds stresses present a source of streaming. A further attribute of the cochlear travelling wave system is the rapid decrease in wave speed and wavelength along the BM and the nearly instantaneous decay of velocity amplitudes once the characteristic place has been passed.

Steady streaming has long been suspected to be present in the cochlea. Already the so-called Békésy eddies, which were observed *in vitro* many decades ago (Békésy 1960; also figure 4 in Lesser & Berkley 1972), suggested the presence of a slow steady streaming flow on top of a primary travelling wave system with higher flow velocities. Streaming has been explicitly mentioned by Lesser & Berkley (1972) who presented a model of a passive cochlea based on two-dimensional potential flow. The linear nature of the governing equations in their model and the absence of viscous boundary layers naturally prevented the occurrence of streaming phenomena apart from Stokes drift. Lighthill (1992) was the first (and to the best of the authors' knowledge still the only) author to provide tangible theoretical results on streaming in the cochlea. His work was strictly of theoretical nature and provided a set of surprisingly simple and elegant results predicting the streaming motion in a harmonically stimulated cochlea.

As pointed out by Lighthill (1992), steady streaming in the cochlea might lead to a force which deflects the hair bundles of the inner hair cells. Since mechanical bending of these hair bundles triggers the nerve signals which lead to hearing, a direct impact of streaming on the hearing sensation is possible. Further physiological effects related to streaming will be discussed later in this work.

Despite the potential relevance of steady streaming to the hearing process, this topic has found only little attention until recently (e.g. Böhnke & Scharff 2009; Gerstenberger & Wolters 2011). Kotas, Rogers & Yoda (2011) performed an experimental study on the streaming in the inner ear of fish and investigated whether streaming might stimulate the hair cells of the otoliths (linear balance sense). To the best of the authors' knowledge, the only available numerical results on streaming in the human cochlea are due to Gerstenberger (2013). A critical discussion of Lighthill's predictions is still outstanding.

It is the aim of the present article to investigate steady streaming in the cochlea and to illustrate and verify Lighthill's predictions on the basis of a computational model. The different components of steady streaming will be shown, i.e. Eulerian and Lagrangian streaming flows and the Stokes drift. Differences between results of our model and Lighthill's predictions shall be critically discussed. In particular, we will investigate the contribution of the BM motion to Eulerian streaming.

For the present study, we will use a two-dimensional box model which includes the scala vestibuli, the scala tympani and the BM. It neglects the other fluid spaces and membranes (e.g. the scala media with the Corti organ, cf. figure 1*b*) as well as the coiled shape of the cochlea. The small Reynolds numbers present in the cochlea suggest that the coiling is irrelevant to the phenomena studied here. However, neglecting the scala media and the Corti organ limits the applicability of our results. In particular, we will be unable to apply our results directly to the deflection of the inner hair cell bundles (see also the discussion in § 4.4). Nevertheless, the present morphological simplifications will allow us to obtain a better understanding of the global mechanics within the cochlea which are relevant to trigger the microscopic phenomena present in the Corti organ.

Furthermore, the used model for the cochlea does not take into account the active processes in the outer hair cells which yield a nonlinear amplification of the local travelling wave amplitudes. Our model belongs to the class of passive two-dimensional box models of the cochlea which are often used to study basic cochlear mechanics (Beyer 1992; Pozrikidis 2008; Edom *et al.* 2013). The mathematical description of the model is based on first principles (Navier–Stokes equations for the fluid, linearly elastic model for the BM). The idealizations in this model (e.g. neglect of the scala

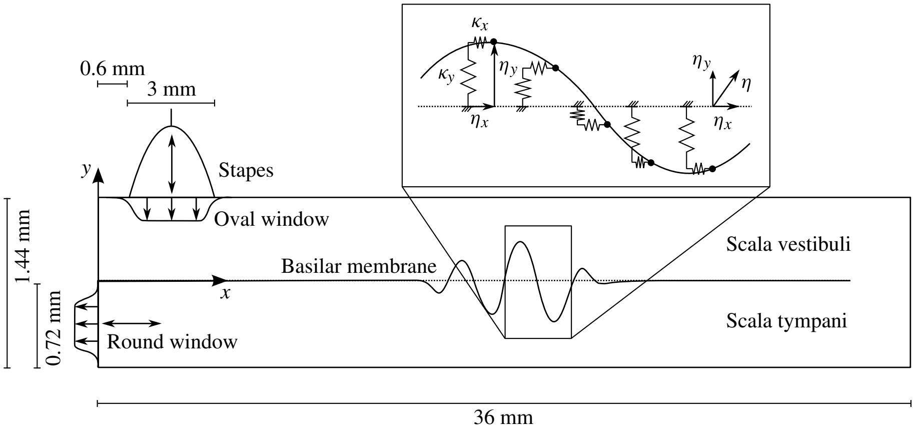

FIGURE 2. Schematic drawing of the two-dimensional box model of the cochlea.

media and the Corti organ) allow only for rough estimates of the strength of the streaming motion in a real cochlea. For a detailed quantification of cochlear streaming further phenomena, such as active amplification, have to be included. Nevertheless, the present study will provide a good illustration of the streaming phenomena present in a cochlea and shall help to further assess the relevance of steady streaming to the hearing process.

The following section (§ 2) describes the computational model used for this study. The primary wave system which results from the interaction between the cochlear fluids and the compliant BM will be described in § 3.1. This section also provides a model validation by demonstrating that the well-known travelling wave phenomenon in the cochlea is reproduced. Section 3.2 presents numerical results for the steady streaming where we will distinguish between Eulerian and Lagrangian streaming fields and the Stokes drift. Sections 3.3 and 3.4 discuss phenomena beyond the common concept of steady streaming: the presence of higher harmonics in the flow fields and a steady displacement of the BM. In § 4.1, the numerical results will be compared with the predictions by Lighthill. Section 4.2 assesses the different mechanisms which lead to steady streaming in the cochlea. Sections 4.3 and 4.4 discuss the magnitude of the streaming in a real cochlea and the possible physiological consequences of streaming. Section 5 concludes the paper.

2. Two-dimensional box model of a passive cochlea

2.1. *Governing equations*

We study the flow field in a two-dimensional box model of the cochlea (figure 2) with a linearly elastic BM. The fluid motion is described by the Navier–Stokes equations for an incompressible flow,

$$\nabla \cdot \boldsymbol{u} = 0, \tag{2.1}$$

$$\rho \frac{\partial \boldsymbol{u}}{\partial t} + \rho\,(\boldsymbol{u} \cdot \nabla)\,\boldsymbol{u} = -\nabla p + \mu \nabla^2 \boldsymbol{u} + \boldsymbol{q}, \tag{2.2}$$

where $\boldsymbol{u} = (u, v)$ denotes the velocity vector, t the time, p the pressure, ρ and μ the density and the dynamic viscosity of the cochlear fluids, respectively; $\boldsymbol{q}$ is a force density which will be used to introduce the effect of the BM on the fluid motion. The coordinate directions x and y are oriented along the BM (axial direction) and perpendicular to it (transversal direction), respectively, with the origin located at the basal end of the BM.

No-slip boundary conditions are imposed at the outer walls and at the BM. At the oval and the round window we impose harmonically oscillating inflow and outflow velocities (perpendicular to the wall) to model the acoustic stimulation. We neglect the small displacements of the two windows because their influence on the resulting primary wave system is negligible.

The BM is modelled by an array of independent oscillators, positioned along the BM. In typical cochlear models, these oscillators are governed by an equation of the type

$$m\frac{\partial^2 \boldsymbol{\eta}}{\partial t^2} + \boldsymbol{R}\frac{\partial \boldsymbol{\eta}}{\partial t} + \boldsymbol{K}\boldsymbol{\eta} = -\Delta p \cdot \frac{\boldsymbol{\eta}}{|\boldsymbol{\eta}|} \tag{2.3}$$

where $\boldsymbol{\eta}(x, t) = (\eta_x(x, t), \eta_y(x, t))$ denotes the displacement of the BM with respect to its resting position. The parameter $m(x)$, and the tensors $\boldsymbol{R}(x)$, and $\boldsymbol{K}(x)$ describe the mass, damping and stiffness per unit area of the BM, respectively, and $\Delta p(x)$ is the pressure difference across the BM. Similar approaches for the BM model have been used, e.g., by Peterson & Bogert (1950) and Lesser & Berkley (1972). Note that neighbouring points in this model of the BM have no mechanical connection apart from an indirect coupling through the surrounding fluid. This idealization is justified by the highly anisotropic mechanical properties of the BM. The BM is not a membrane in the usual mechanical sense; we should rather think of it as an array of individually supported cantilever beams which are oriented perpendicularly to the x–y plane (Baker *et al.* 2006).

In the present model, the inertia m of the BM is negligible in comparison with the inertia of the fluid that is displaced by the BM (virtual mass). Therefore, we choose $m = 0$ which is also in agreement with findings by de la Rochefoucauld & Olson (2007) for small to moderately high frequencies. Furthermore, we assume that the majority of the energy dissipation takes place in the thin Stokes boundary layers that are forming on the BM. Therefore, the structural damping of the BM is neglected as well ($\boldsymbol{R} = 0$) such that no further modelling of this parameter is required. The remaining stiffness tensor $\boldsymbol{K}$ defines a linearly elastic behaviour of the BM.

According to the no-slip boundary condition, the BM motion must be equal to the fluid motion at the BM,

$$\frac{\partial \boldsymbol{\eta}}{\partial t} = \boldsymbol{u}|_{BM}. \tag{2.4}$$

The elastic reaction of the displaced BM leads to a force density $\boldsymbol{q}|_{BM}$ which acts on the flow field along the BM manifold. In line with (2.3), we compute this force as

$$\boldsymbol{q}|_{BM} = -\begin{pmatrix} \kappa_x & 0 \\ 0 & \kappa_y \end{pmatrix}\begin{pmatrix} \eta_x \\ \eta_y \end{pmatrix}. \tag{2.5}$$

The description of the BM motion by (2.4) and (2.5) is a mobility formulation for fluid–structure interaction. It translates naturally into the immersed boundary approach that we will be using for the numerical implementation of the cochlea model (§ 2.2).

Because the density and the viscosity of cochlear fluids are known to be similar to those of water ($\rho = 10^3$ kg m^{-3}, $\mu = 10^{-3}$ kg m^{-1} s^{-1}; Baker *et al.* 2006), the BM stiffness coefficients κ_x and κ_y remain the only physical parameters that have to be modelled. According to common practice in cochlear modelling, we assume that the transversal stiffness κ_y decays exponentially along the x-axis such that we obtain a logarithmic distribution of the resonance frequencies along the BM with 20 kHz at the base of the cochlea and 20 Hz at the apex,

$$\kappa_y(x) = 6.25 \times 10^{11} \cdot \exp(-x/2.606\ \text{mm})\ (\text{N m}^{-3}). \tag{2.6}$$

The axial stiffness κ_x of the BM elements has not been quantified conclusively so far in the literature such that our model must rely on rough estimates. Here, we assume that the axial stiffness is 100 times lower than the transveral stiffness, i.e. $\kappa_x = \kappa_y/100$. This choice is motivated by the microstructure of the BM (e.g. figure 2 in Wittbrodt, Steele & Puria 2006) which may lead to such an anisotropy. A decay in of the axial stiffness toward the apex of the cochlea has been observed in experiments by Emadi, Richter & Dallos (2004). Despite the relatively low axial stiffness, we will see (§ 3.1) that the axial displacements of the BM are approximately two orders of magnitude smaller than its transversal displacements. Moreover, it turns out that the observed phenomena are fairly robust with respect to the actual choice of κ_x. An axial coupling between neighbouring BM elements (Naidu & Mountain 2001) is not included in our model.

The outer dimensions of the box model (figure 2) are 36 mm in length and 1.44 mm in height. These dimensions were selected following Lighthill (1981) because results from this model will be compared with Lighthill's predictions. The BM is placed in the middle of the box and extends from the base of the cochlea over a length of 35 mm. The resulting 'hole' at the apex corresponds to the so-called helicotrema which connects the two fluid spaces above and below the BM.

The oval and round windows are located on the top wall of the box at $0.6 \leqslant x \leqslant 3.6$ mm and on the front wall at $0.12 \leqslant y \leqslant 0.54$ mm, respectively. We assume rectangular wall-normal velocity profiles at these windows (smoothed at the ends) to prescribe an inflow and outflow due to vibration of the stapes (middle ear ossicle). These velocities are varied harmonically with frequency f and amplitude U_{in} to simulate a pure tone stimulation of the cochlea. The rectangular shape for the velocity profile at the oval window is justified by the solid plane footplate of the stapes which pushes onto the membrane-covered oval window. The round window, however, is covered by a supple membrane and most likely does not deform in a rectangular shape. Nevertheless, we believe that the effects of this idealization on the streaming motion remains negligible, because the steady streaming is strongest close to the BM at the characteristic place which is typically far from the round window.

2.2. *Numerical implementation*

The governing equations are solved with a high-order solver for the Navier–Stokes equations (Henniger, Obrist & Kleiser 2010) which uses a third-order explicit Runge–Kutta integration scheme in time and up to sixth-order finite differences in space on a staggered Cartesian grid. The mesh width is reduced close to the walls and the BM to resolve the boundary layers. The solver has been thoroughly validated for different fluid dynamical problems (Henniger *et al.* 2010). Typical simulations use grids with 320×9216 points and roughly 60 000 time steps to simulate approximately 25 ms (for a 1000 Hz stimulation). The turnaround time for one such simulation was approximately 400 h on eight cores of a personal computer with Xeon E5-2643 processors.

The interaction between the fluid and the BM is modelled through an immersed boundary approach. The immersed boundary method (see Peskin 2002) has already been used in the field of cochlear mechanics by Beyer (1992) and Givelberg & Bunn (2003). Our approach implements the mobility formulation (2.4) and (2.5). To this end, the manifold which represents the BM is discretized by an immersed one-dimensional grid with roughly the same number of points as we use for the fluid grid in the axial direction. The velocity $\boldsymbol{u}|_{BM}$ on the right-hand side of (2.4) is interpolated from the fluid grid onto the immersed grid with a bilinear scheme. Equation (2.4) is then advanced to the next time step with the same explicit Runge–Kutta scheme as used for the Navier–Stokes equations. This yields the new position $\boldsymbol{\eta}$ of the BM from which we compute the force density $\boldsymbol{q}|_{BM}$ according to (2.5). This field force density is distributed to the surrounding fluid grid points again by a bilinear scheme.

The bilinear interpolation limits the overall order of convergence of our numerical model. Nevertheless, validation tests have shown that the numerical errors introduced by our fluid–structure interaction scheme remain below the overall level of accuracy of the flow solver.

The simulations are started from a zero initial condition for the flow field and the BM at its resting position. The amplitude of the harmonic stimulation at the oval window is slowly ramped up over the first 12 oscillations. In the following, we will present only results after a statistically steady flow field has been reached, such that the numerically computed mean flow fields are independent of the time at which they have been evaluated. Such a state is typically reached to a sufficient level of accuracy after approximately 25 periods of the harmonic stimulation.

3. Results

In this section, we present results from our numerical model. Unless stated otherwise, the simulations used a stimulation of the cochlea with $f = 1000$ Hz and $U_{in} = 30\ \mu\text{m s}^{-1}$ at the oval window. These values are equivalent to an acoustic signal of approximately 76 dB ear canal pressure according to measurements by Sim *et al.* (2010). In our model, the characteristic place (where the maximum BM amplitude is found) for this stimulation is at $x_c \approx 14.4$ mm.

If we use the long axis of the stapes footplate (3 mm) as typical length scale L and U_{in} as a reference velocity, this stimulation leads to a Reynolds number of $Re = U_{in}L/\nu = 0.09$ and a Womersley number of $\alpha = L\sqrt{\omega/\nu} \approx 238$ (where $\nu = \mu/\rho$ and $\omega = 2\pi f$). This suggests that the effects of the advective terms of the Navier–Stokes equations are weak and that the flow features very thin Stokes boundary layers.

3.1. *Primary travelling wave system*

The results in figures 3(*a*) and 4 confirm that a harmonic stimulation of the cochlea leads to travelling waves in the fluid as well as on the BM. In the context of steady streaming, we denote this travelling wave as the primary wave system which oscillates at the fundamental frequency f. The phase velocity c_{ph} of the travelling wave propagating toward the apex is of the order of 1 m s^{-1} at the characteristic place and goes rapidly to zero shortly beyond that point. The amplitude of the BM deflection at the characteristic place increases for lower frequencies (figure 3*b*). The maximum BM deflection remains several orders of magnitude below the overall dimensions of the cochlea for all relevant acoustic stimulations. These results serve as a basic validation of our computational model because they are in good agreement with

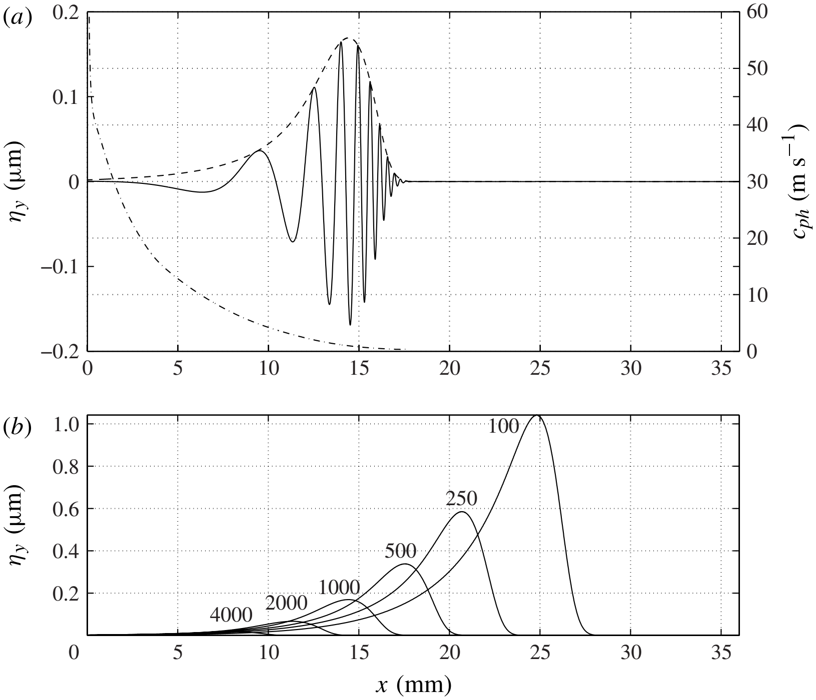

FIGURE 3. Travelling waves on the BM: (*a*) amplitude (– – –) and instantaneous deflection (——) of the transversal BM displacement η_y at 1000 Hz, phase velocity (–·–) of the travelling wave (right axis). (*b*) Amplitudes of the transversal displacement η_y for different stimulation frequencies indicated in Hertz.

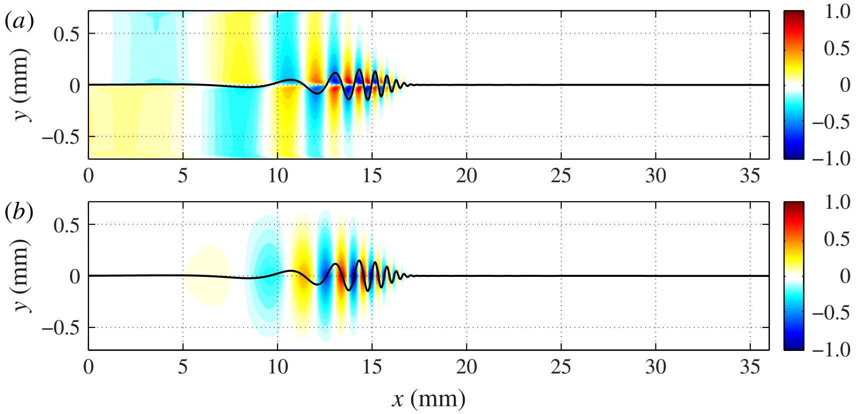

FIGURE 4. Velocity components (in mm s^{-1}) of the instantaneous flow field when the stapes is moving out of the cochlea with a maximum velocity of 30 µm s^{-1} (—— exaggerated BM displacement; for the true magnitudes see figure 3). (*a*) Axial velocity u. (*b*) Transversal velocity v.

the well-established concept of travelling waves (Békésy 1960) in passive cochlear mechanics.

The fluid velocities in the travelling wave (figure 4) increase towards the characteristic place and are highest close to the BM. They are one to two orders of magnitude larger than the stapes velocity amplitude U_{in}. Beyond the characteristic place, nearly no fluid motion is found. At the bounding walls and at the BM, we observe thin Stokes boundary layers whose thickness scales with $\sqrt{\nu/\omega}$. For very high frequencies the Stokes boundary layers become very thin such that the bulk flow of the primary wave system may be described as a potential flow (Lesser & Berkley 1972). In order to include the Stokes boundary layers in the primary wave system, it would be sufficient to solve the (unsteady) Stokes equations because the small scales of travelling waves lead to Reynolds numbers well below unity. For studying steady streaming, however, it is necessary to include also the nonlinear advective terms and therefore we solve the full Navier–Stokes equations.

3.2. *Eulerian and Lagrangian mean flow fields*

As pointed out by many authors, e.g. Riley (2001), it is important to distinguish between Eulerian and Lagrangian streaming velocities. The Eulerian mean velocity refers to the average velocity at a fixed point in space, whereas the Lagrangian mean velocity refers to the average velocity of a fluid particle along its trajectory. The calculation of the Eulerian mean flow field $\boldsymbol{u}_E$ is straightforward and consists of the temporal average of the fluctuating velocity field over one period of the fundamental oscillation $T = 1/f$,

$$\boldsymbol{u}_E(\boldsymbol{x}) = \overline{\boldsymbol{u}(\boldsymbol{x})} = \frac{1}{T}\int_{t-T}^{t} \boldsymbol{u}(\boldsymbol{x}, t')\,\mathrm{d}t'. \tag{3.1}$$

The computation of the Lagrangian mean flow $\boldsymbol{u}_L$ is more involved. We define it as the ratio of the distance $\Delta\boldsymbol{x}$ and the period T,

$$\boldsymbol{u}_L = \Delta\boldsymbol{x}/T, \tag{3.2}$$

where $\Delta\boldsymbol{x} = \boldsymbol{x}_p(t) - \boldsymbol{x}_p(t - T)$ is the distance travelled by a fluid particle over the period T and

$$\boldsymbol{x}_p(t) = \boldsymbol{x}_p(0) + \int_0^t \boldsymbol{u}(\boldsymbol{x}_p(t'), t')\,\mathrm{d}t'. \tag{3.3}$$

Following Lighthill (1992), we define the difference between the Lagrangian and the Eulerian mean as $\boldsymbol{u}_M = \boldsymbol{u}_L - \boldsymbol{u}_E$. It is synonymous to the well-known Stokes drift. This component of the streaming originates from local gradients in the primary wave. If we assume that $\boldsymbol{u}(\boldsymbol{x}, t) = \overline{\boldsymbol{u}(\boldsymbol{x})} + \mathrm{Re}\{\hat{\boldsymbol{u}}(\boldsymbol{x})\exp(\mathrm{i}\omega t)\}$ (where $\mathrm{Re}\{\cdot\}$ indicates the real part of a complex number) and that the velocity magnitude is sufficiently small, it can be derived from (3.3) that the Stokes drift is given by

$$\boldsymbol{u}_M = -\mathrm{Re}\left\{\frac{\mathrm{i}(\nabla\hat{\boldsymbol{u}})^*\hat{\boldsymbol{u}}}{2\omega}\right\} \tag{3.4}$$

where $\hat{\boldsymbol{u}}(\boldsymbol{x})$ is some complex amplitude function and the superscript * denotes the complex conjugate Lighthill (1992).

Figures 5(*a*) and 6(*a*) show the Eulerian and the Lagrangian streaming flow fields, $\boldsymbol{u}_E$ and $\boldsymbol{u}_L$, respectively. Both flow fields consist of a pair of vortices whose centres are approximately aligned with the characteristic place at $x_c \approx 14.4$ mm. The vortex above the BM rotates in the counterclockwise direction, opposite to the vortex beneath the BM. The highest streaming velocities are found close to the BM and are approximately 4.75 $\mu\mathrm{m\ s}^{-1}$ ($\approx$15 % of the maximum stapes velocity U_{in}) for the Eulerian field and approximately 1 $\mu\mathrm{m\ s}^{-1}$ or 4 % of U_{in} for the Lagrangian field.

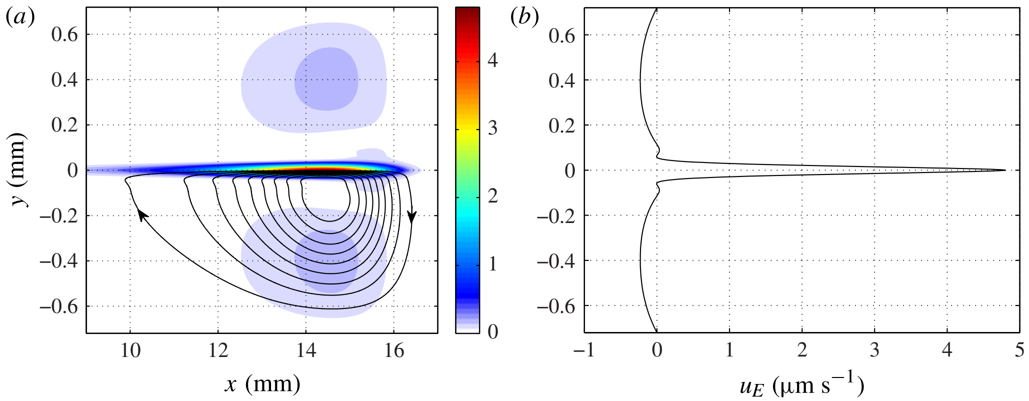

FIGURE 5. Eulerian mean flow field $\boldsymbol{u}_E$: (*a*) magnitude and streamlines (in µm s^{-1}); (*b*) axial velocity profile $u_E(x_c, y)$ taken at the characteristic place.

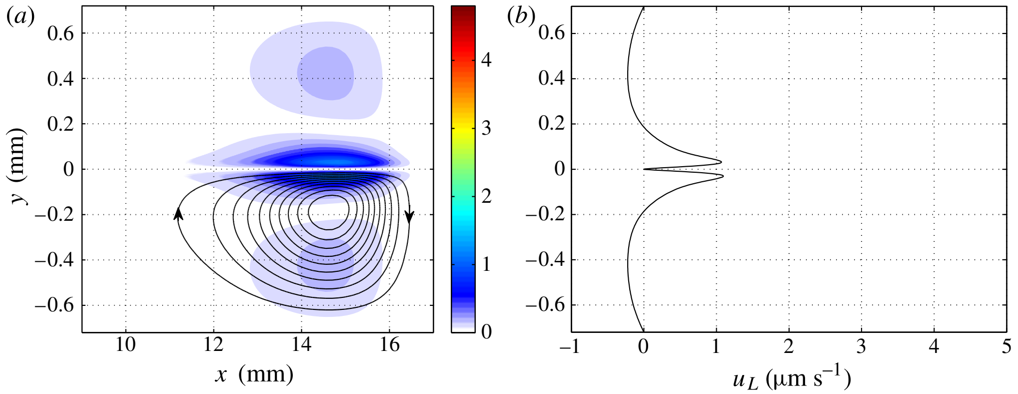

FIGURE 6. Lagrangian mean flow field $\boldsymbol{u}_L$: (*a*) magnitude and streamlines (in µm s^{-1}); (*b*) axial velocity profile $u_L(x_c, y)$ taken at the characteristic place.

The axial streaming profiles $u_E(x_c, y)$ and $u_L(x_c, y)$ at the characteristic place (figures 5*b* and 6*b*) highlight the differences between the two mean velocities in the boundary layer region. The Eulerian mean velocity drops rapidly from its maximum value at $y=0$ to nearly zero at the edge of the Stokes layer, whereas the Lagrangian mean velocity increases from zero at the BM to a maximum within the boundary layer. In the bulk flow region, the two mean velocities have approximately the same values. The Lagrangian mean velocity at the resting position of the BM ($y=0$) is exactly zero because the elements of the BM are elastically fixed to a given location such that they cannot drift (apart from a steady axial displacement attained during the transient phase, see § 3.4). The Eulerian mean velocity, however, is non-zero at $y=0$ which reflects the fact that the oscillating BM is generally either above or below its resting position.

Finally, figure 7 shows the Stokes drift $\boldsymbol{u}_M=\boldsymbol{u}_L-\boldsymbol{u}_E$. The Stokes drift at the resting position of the BM exactly cancels the Eulerian streaming such that the Lagrangian mean velocity of the BM becomes zero. As a consequence, the vortices due to the Stokes drift rotate opposite to the Lagrangian and the Eulerian vortices.

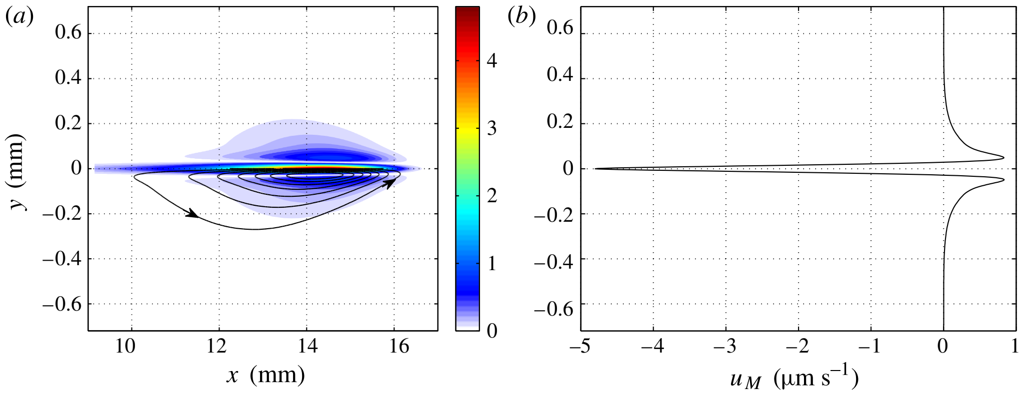

FIGURE 7. Stokes drift $\boldsymbol{u}_M = \boldsymbol{u}_L - \boldsymbol{u}_E$: (*a*) magnitude and streamlines (in μm s^{-1}); (*b*) axial velocity profile $u_M(x_c, y)$ taken at the characteristic place.

3.3. *Higher harmonics*

We can observe a phenomenon closely related to steady streaming when we study the trajectory of a point on the BM itself (figure 8*a*). This trajectory has the shape of a figure of eight or of a Lissajous figure with frequency ratio 2:1 and a 90° phase shift. In fact, the axial velocity oscillates at twice the fundamental frequency while the transversal motion follows the fundamental frequency. Apparently, the weak nonlinear phenomena which lead to streaming have injected energy into a higher harmonic rather than into the zero frequency.

In general, higher harmonics will always be present as soon as quadratic nonlinear terms (such as the advective terms of the Navier–Stokes equations) are involved. However, these components are usually not noticed because they are of much smaller amplitude than the oscillations in the primary wave system. In this symmetric set-up with an elastically supported mechanical structure, the axial component of the primary wave system is exactly zero in the plane of symmetry such that the higher harmonics are visible.

The trajectories of fluid particles only a little bit away from the BM are slender ellipses and become circles in the bulk flow (figure 8*b*). These trajectories show no obvious effects of higher harmonics because the axial oscillation at the fundamental frequency is now dominant and masks the higher harmonic motion.

Finally, we would like to point out that the fluid trajectories are not closed (not visible in figure 8) due to the non-zero Lagrangian mean velocity, whereas the BM trajectories are closed because $\boldsymbol{u}_L|_{y=0} = 0$.

3.4. *Steady displacement of the BM*

We stretch the concept of steady streaming further by considering the axial displacement of the BM (figure 9). The axial oscillation of the BM has its highest amplitude close to the characteristic place. In contrast to the transversal displacement, the displacement in the axial direction has a non-zero mean. This mean displacement results in an axial stretching of the BM away from the characteristic place to either side (cf. figure 8*a*). It is the result of an axial drift during the transient period while the flow is transitioning from its initial state toward the steady-state oscillating configuration.

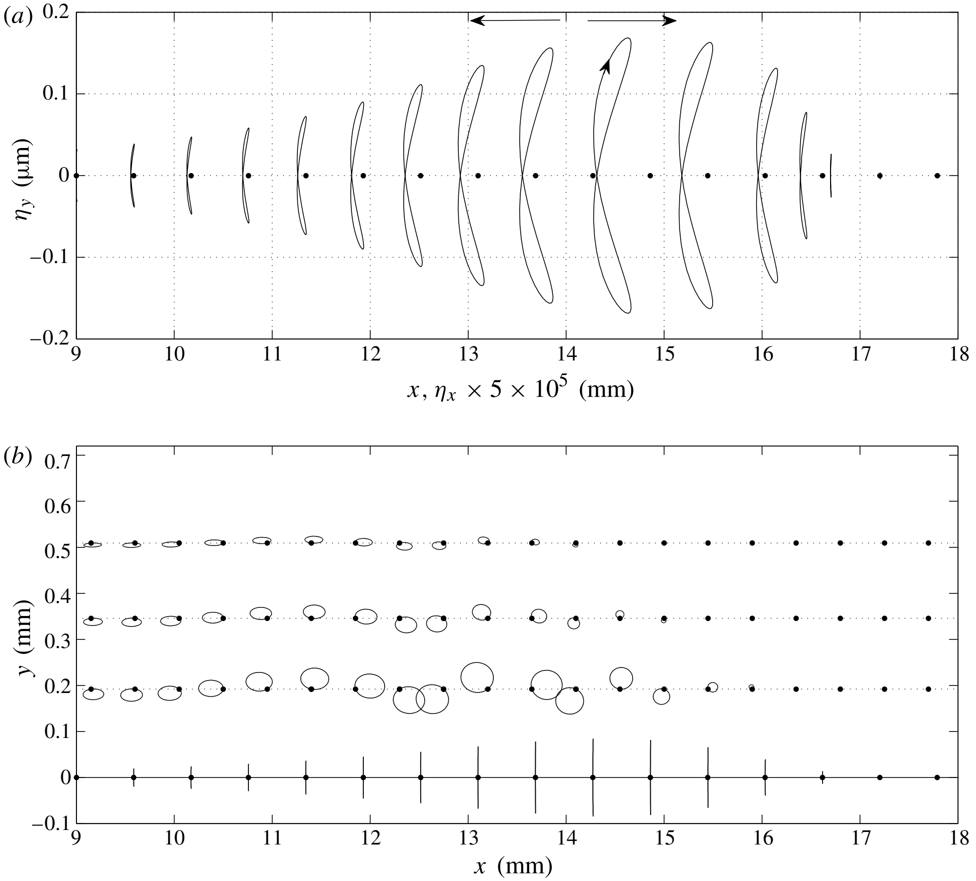

FIGURE 8. (*a*) Trajectories of BM elements (——) during one oscillation (● positions of the elements in the relaxed BM). To highlight the figure-of-eight shape of the trajectories, the aspect ratio of the trajectories is stretched in the axial direction. The arrows indicate the steady axial BM displacement away from the characteristic place at $x_c \approx 14.4$ mm. (*b*) Trajectories of fluid and BM elements (——) with starting positions (●). The size of the trajectories is strongly exaggerated for visibility, while the correct aspect ratio is maintained in this panel.

This net displacement causes steady axial elastic forces pointing toward the characteristic place. Apparently, there must exist a balance between these restoring forces and the steady streaming forces which act on the BM. Section 4.2.1 will offer an explanation for this phenomenon.

In general, the axial displacement η_x is two orders of magnitude below the transversal displacement η_y although the axial stiffness is significantly smaller than the transversal stiffness. Further numerical experiments showed that the magnitude of the net BM displacement is inversely proportional to the axial stiffness κ_x of the BM. Therefore, the steady axial restoring forces are independent of the axial stiffness. It also follows that the phenomenon of the axially stretched BM occurs independently of our particular choice of the ratio κ_y/κ_x (assuming that the axial stiffness is sufficiently high such that the axial displacements remain small compared with the wavelengths of the travelling wave).

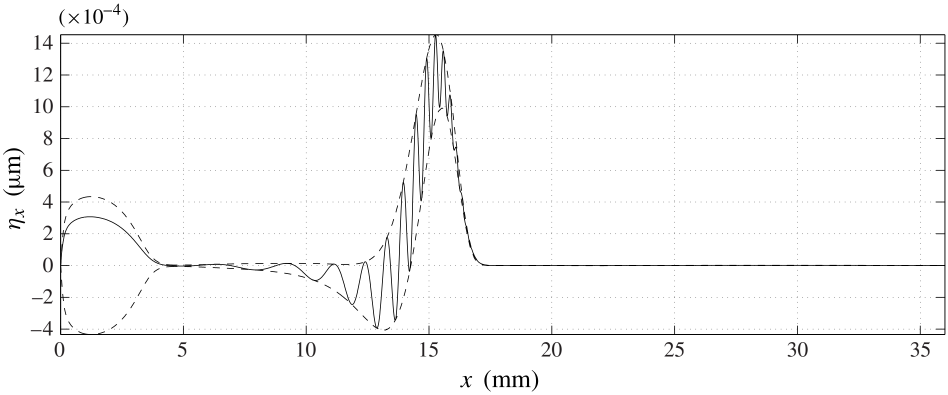

FIGURE 9. Axial BM displacement η_x: envelope (– – –) and instantaneous deflection (——).

4. Discussion

4.1. *Comparison to Lighthill's results*

Lighthill (1992) provides a number of analytical results for the flow field of the primary wave system and of the various streaming fields. These results are given in function of the wavenumber $k(x)$ and the transversal velocity amplitude $V(x)$ of the travelling wave on the BM. These values can be determined with the help of the Hilbert transform of the instantaneous BM displacement (Huang *et al.* 1998). In the following, we will compare our numerical results with Lighthill's predictions where we use the wavenumbers and transversal velocity amplitudes obtained from our simulations (cf. figure 3). We will find that there is a remarkable agreement between Lighthill's predictions and most of our numerical results. Only for the so-called slip velocity (§ 4.2.1) do we observe significant differences. We will discuss this observation in detail and describe an additional source of streaming, which may explain the differences to Lighthill's predictions.

4.1.1. *Primary wave system*

Lighthill gives a general solution [A 4] (we use brackets, [·], to refer to equations in Lighthill 1992) for the primary wave system which divides the fluid motion into an external irrotational flow and a Stokes boundary layer. If we apply the wavenumber $k(x)$ and the amplitude $V(x)$ from our simulation to Lighthill's theoretical results, they agree very well with our numerical results in the vicinity of the characteristic place (figure 10). Small differences arise mainly due to the Stokes layers at the bounding walls of the cochlea which were neglected by Lighthill. Furthermore, Lighthill (1992) writes $\exp[\mathrm{i}(\omega t - kx)]$ for the travelling wave assuming only small changes either in k or in x. Since the wavenumber increases exponentially along the BM (cf. figure 3*a*), we changed the original term to $\exp[\mathrm{i}(\omega t - \int k\, \mathrm{d}x)]$.

Away from the characteristic place, the differences between our results and Lighthill's predictions increase because of the increasing influence of the bounding walls and of the round and oval windows. We assume that these differences are not relevant for the streaming motion because they arise at some distance from the characteristic place where the largest streaming effect is present.

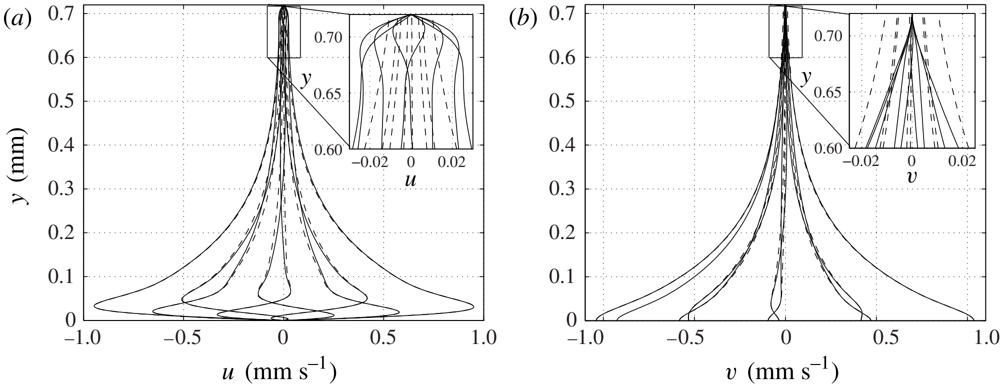

FIGURE 10. Instantaneous velocity profiles at the characteristic place taken at $t = t_0 + nT/8$, $n = 0, 1, \dots, 7$ (—— simulation; – – – analytical prediction, equation [A 4]). (*a*) Axial velocity u. (*b*) Transversal velocity v.

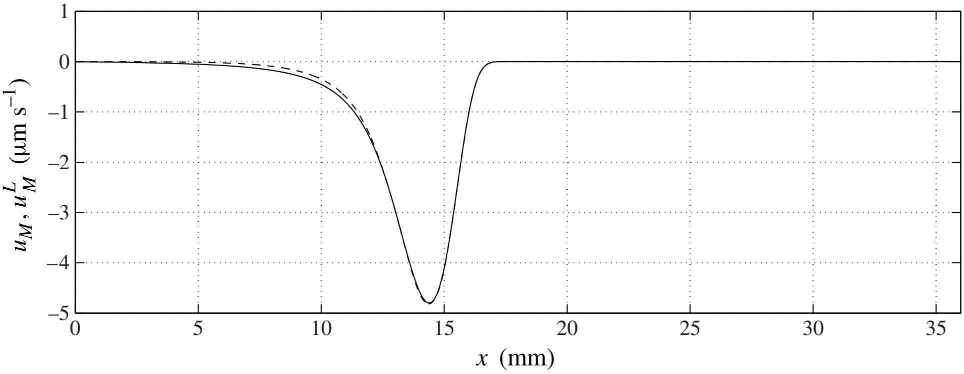

FIGURE 11. Stokes drift u_M at $y = 0$: —— simulation; – – – analytical prediction (4.1) according to Lighthill (1992).

4.1.2. *Stokes drift*

Lighthill's predictions for the Stokes drift $\boldsymbol{u}_M^L = (u_M^L, v_M^L)$ again depend on the wave number and the velocity amplitude of the travelling wave. For the Stokes drift at the resting position $y = 0$ of the BM, Lighthill predicts ([75], [B 17])

$$u_M^L|_{y=0} = -\frac{V^2}{\sqrt{8\nu\omega}}, \qquad v_M^L|_{y=0} = 0. \tag{4.1a,b}$$

Figure 11 shows that the axial Stokes drift at $y = 0$ according to (4.1) agrees very well with our results. The transversal drift $v_M|_{y=0}$ in our model is of the order of 10^{-2} μm s^{-1}. This small deviation from (4.1) can be attributed to the asymmetric placement of the oval and round windows (cf. figure 2).

The axial velocity profile $u_M(x_c, y)$ at the characteristic place (figure 7*b*) is practically identical to the analytically predicted velocity profile [B 13] by Lighthill (1992). Because the analytical result assumes no boundaries other than the BM, both curves differ necessarily close to the bounding wall. Furthermore, Lighthill states that

$v_M^L = 0$ everywhere in his unbounded domain. In our model, the transversal streaming velocity v_M must be non-zero in general because the bounding walls at the base and at the apex lead to a two-dimensional flow such that conservation of mass can be satisfied (cf. figure 7*a*).

4.1.3. *Slip velocity*

Lighthill derives a slip velocity u_S^L for the Eulerian mean motions. This slip velocity is measured at the edge of the Stokes boundary layer of the BM and reflects the contributions of the Reynolds stresses to the Eulerian streaming. It can be understood as a non-zero boundary condition for the bulk flow. Lighthill predicts in equation [92] that

$$u_S^L = \frac{V^2 k}{4\omega} - \frac{3VV'}{4\omega}, \tag{4.2}$$

where $V' \equiv \mathrm{d}V/\mathrm{d}x$. The first term in (4.2) as well as part of the second term $(-VV'/4\omega)$ are due to the Reynolds shear stresses $-\rho\overline{u'v'}$ where u' and v' are the fluctuating components of the velocity field $(u, v) = (\overline{u}, \overline{v}) + (u', v')$ and the line indicates an average according to (3.1). The remainder of the second term $(-VV'/2\omega)$ is due to the normal Reynolds stresses $-\rho\overline{u'^2}$.

The Eulerian streaming field from our simulations (figure 5) does not agree with these predictions. Moreover, it is difficult to make out a distinct edge of the Stokes boundary layer where u_S^L would apply (cf. figure 5*b*). We will discuss this issue in detail in the following section where we will also provide an explanation for this apparent mismatch.

4.2. *Sources of steady streaming*

The present section discusses the sources of the streaming motion, concentrating on the comparisons between our results and Lighthill's predictions. On the one hand, we have seen that there is a remarkable agreement for the primary wave system as well as for the Stokes drift. Therefore, it appears that Lighthill's formulas yield accurate predictions as long as the velocity amplitude V and the wavenumber k are known for the primary wave system. On the other hand, the discrepancies for the Eulerian mean flow (i.e. in u_S^L) are significant and require further discussion. We will find in the following that there exists an additional source of streaming that was not considered by Lighthill. If we take into account this source which acts in addition to the Reynolds stresses, we find a reasonable agreement with Lighthill's theoretical results.

4.2.1. *Streaming due to moving BM*

We can learn more about the additional source of streaming when we repeat our simulations with the unsteady Stokes equations, i.e. we deliberately neglect the nonlinear advective terms of the Navier–Stokes equations. This eliminates any contribution of the Reynolds stresses to the streaming. The primary wave system in such simulations is almost identical to the primary wave system in the full model. This confirms that the primary wave system is mainly governed by the unsteady Stokes equations. As a consequence, we also obtain nearly the same Stokes drift $\boldsymbol{u}_M$. One might expect that such a simulation does not yield any Eulerian mean flow because there are no (apparent) nonlinearities in the governing equations. However, the Eulerian mean is non-zero (figure 12*a*) and consists of a large pair of vortices aligned with the characteristic place. Apart from the streaming velocity at $y = 0$, the associated axial flow profile (figure 12*b*) is very different from the Eulerian profile

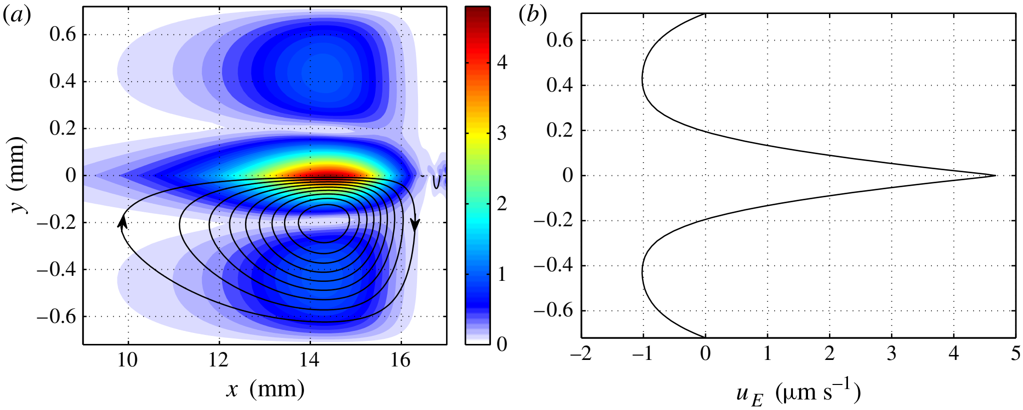

FIGURE 12. Eulerian mean velocity for the unsteady Stokes equations: (*a*) streamlines with velocity magnitude (in μm s^{-1}); (*b*) axial velocity profile at the characteristic place. (The small wiggles in (*a*) at $x \approx 17$ mm are a numerical artefact due to the very slow convergence of the steady state.)

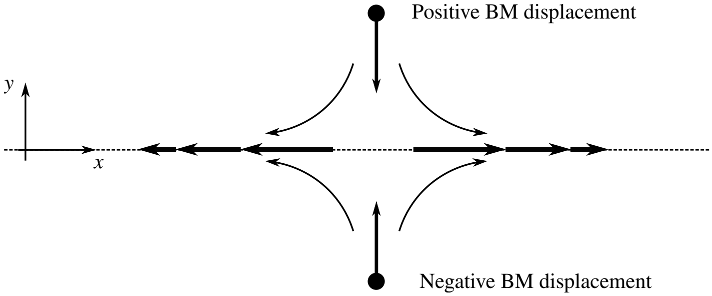

FIGURE 13. Axial stretching induced by a single element of the oscillating BM.

in figure 5(*b*) and does not exhibit any boundary layer length scales (e.g. the Stokes boundary layer length scale $\sqrt{\nu/\omega} \approx 13$ μm).

These results show that there exists a source of streaming other than the Reynolds stresses. It results from the fluid–structure interaction. The equation of motion for the BM, (2.4), together with the reaction forces, (2.5), yields the necessary nonlinearity because these two equations combine the oscillation of the BM with a periodic force acting on the fluid. The schematic in figure 13 explains one aspect of this effect: consider a single element of the BM. When this element oscillates, the elastic reaction force will always point toward the resting position. These reaction forces induce a flow field as indicated in figure 13. While the transversal velocity component of this flow cancels over one period at $y = 0$, the axial velocities at $y = 0$ point away from the BM element during the whole oscillation period. This yields an Eulerian mean flow with a quadrupole-like structure in which the axial velocities point away from the characteristic place and the transversal velocities toward it.

The velocities which are induced by this mechanism are quite small and cannot explain the vortical structures in the Eulerian streaming field in figure 12(*a*). However, this axial streaming is responsible for a slow axial drift of the BM away from the characteristic place. This drift leads to axial restoring forces of the BM which point

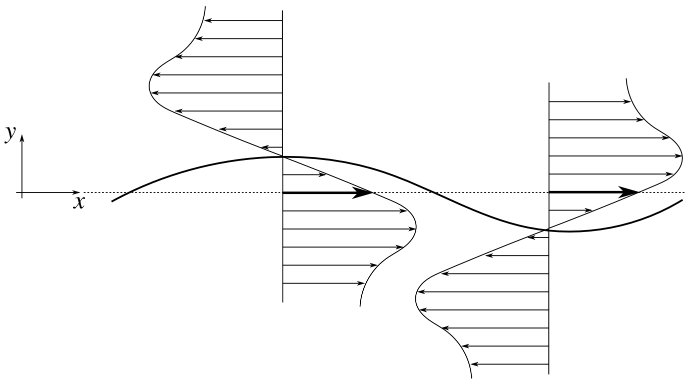

FIGURE 14. Transversally displaced velocity profiles close to the BM. The axial velocities at $y=0$ (bold arrows) are positive most of the time.

toward the characteristic place. Eventually the restoring forces are so large that the axial drift becomes a steady axial displacement (on average over one period). This effect is reflected in the steady axial displacement shown in figures 8(*a*) and 9 (and § 3.4).

To finally explain the Eulerian flow field shown in figure 12 we have to look in more detail at the interaction of the BM displacement with the Stokes boundary layers of the primary wave system. Lighthill (1992) computed the axial velocity profile in the Stokes boundary layer as (according to [63])

$$u_{BL}(x, y, t) = \mathrm{Re}\left\{\mathrm{i}V(x)\left[1-\mathrm{e}^{-y\sqrt{\mathrm{i}\omega/\nu}}\right]\mathrm{e}^{\mathrm{i}(\omega t-kx)}\right\}. \tag{4.3}$$

Note that this formula implicitly assumes that the vibrating BM remains at $y=0$ throughout the oscillation. This approximation appears reasonable for sufficiently small BM displacements. However, it cannot explain the non-zero Eulerian mean at $y=0$ because $u_{BL}(x, 0, t)=0$. Assuming that the BM displacement leads to a small transversal shift η_y of the velocity profiles, a better approximation for the axial velocity is given by $u_{BL}(x, y-\eta_y, t)$. Figure 14 illustrates this shift and shows that it leads to a positive axial velocity at $y=0$ throughout most of the oscillation period. The Eulerian mean at $y=0$ can be computed by linearizing $u_{BL}(x, y-\eta_y, t)$ about $y=0$,

$$u_E|_{y=0} = \frac{1}{T}\int_t^{t+T} u_{BL}(x, y-\eta_y, t')\,\mathrm{d}t' \approx \frac{1}{T}\int_t^{t+T}\left[u_{BL}-\eta_y\frac{\partial u_{BL}}{\partial y}\right]_{y=0}\mathrm{d}t'. \tag{4.4}$$

The first term in the second integral does not contribute to the Eulerian mean, whereas the second term has a non-zero mean. If we take the transversal BM displacement as $\eta_y(x, t)=\mathrm{Re}\{-\mathrm{i}V(x)/\omega\exp[\mathrm{i}(\omega t-kx)]\}$ (Lighthill 1992), we obtain

$$u_E|_{y=0} \approx \frac{V^2}{\sqrt{8\nu\omega}}. \tag{4.5}$$

Apart from the sign, this expression is identical to Lighthill's formula for the Stokes drift at the BM, (4.1). Therefore, the Eulerian streaming due the moving BM exactly cancels the Stokes drift at $y=0$. We will see in the following section that this result has direct implications on Lighthill's prediction for the slip velocity.

The streaming (4.5) can be interpreted as a slip boundary condition along the BM which drives the vortices illustrated in figure 12. This bulk flow is steady and governed by the (steady) Stokes equations. Therefore, it does not exhibit any Stokes boundary layer length scales.

4.2.2. *Streaming due to Reynolds stresses*

The previous section illustrated the presence of an additional source of streaming, but did not explain the discrepancy between Lighthill's slip velocity and our results. We can make further progress by studying the effect of the Reynolds stresses alone. To this end, we have to include again the effect of the nonlinear advective terms of the Navier–Stokes equations (in contrast to § 4.2.1 where these terms were neglected). Furthermore, we modify the model in such a way that the streaming due to the moving BM (as was studied in § 4.2.1) does not take place. We can achieve this by applying the reaction forces of the BM at $y=0$ instead of $y=\eta_y$. Likewise the velocity $\boldsymbol{u}|_{BM}$ on the right-hand side of (2.4) is evaluated at $y=0$. In other words, this modified BM returns the correct reaction forces to the fluid whereas its small transversal displacement within the fluid space is neglected. This is equivalent to a first-order approximation of the actual BM motion. Similar concepts have been used by other authors (e.g. Hill 1995) to model wall roughness by non-zero wall-normal velocities transpiring through a flat wall. Following the reasoning of the previous section, this modification eliminates the streaming source due to the moving BM such that the effect of the Reynolds stresses alone can be studied.

We find that the primary wave system as well as the Stokes drift remain nearly unchanged in this modified model. This confirms that our modifications only affect the Eulerian streaming. The gradients of the resulting Reynolds stresses are shown in figure 15. These quantities can be understood as force densities which drive the Eulerian streaming of this modified model.

Figure 15 shows that the main contribution to streaming comes from the axial shear stress term $-\rho\,\overline{v'\,\partial u'/\partial y}$ (figure 15*b*) whereas the contribution $-\rho\,\overline{u'\,\partial u'/\partial x}$ of the axial normal stresses (figure 15*a*) is negligible. The transversal Reynolds stress components $-\rho\,\overline{u'\,\partial v'/\partial x}$ and $-\rho\,\overline{v'\,\partial v'/\partial y}$ (figure 15*c*,*d*) are of nearly equal magnitude and are weaker than the axial shear stress term.

The force density fields in figure 15 lead to the Eulerian mean flow shown in figure 16. It consists of a pair of vortices which rotate in the opposite(!) sense to the vortices in the original model (cf. figure 5*a*). The effect of the Reynolds stresses is concentrated within the boundary layer and leads to the (negative) peak at the edge of the boundary layer (figure 16*b*). The velocity at this point can be identified with Lighthill's slip velocity, nevertheless the prediction u_S^L still differs significantly from this velocity. The reason is simply that Lighthill assumed that the Eulerian streaming due to the Reynolds stresses must compensate for the Stokes drift at $y=0$. Therefore, he imposed $V^2/\sqrt{8\nu\omega}$ as a boundary condition (equation [80]). We know from the previous section that this is not the right choice because the Stokes drift at $y=0$ is already compensated for by the Eulerian mean flow (4.5) due to the moving BM. Figure 16(*b*) confirms that the Eulerian mean flow due to the Reynolds stresses is zero at $y=0$. Therefore, Lighthill's derivation for the slip velocity has to be repeated with a homogeneous boundary condition at $y=0$. This leads to the corrected slip velocity

$$u_S=\frac{V^2k}{4\omega}-\frac{3VV'}{4\omega}-\frac{V^2}{\sqrt{8\nu\omega}} \tag{4.6}$$

where the third term is new compared with (4.2).

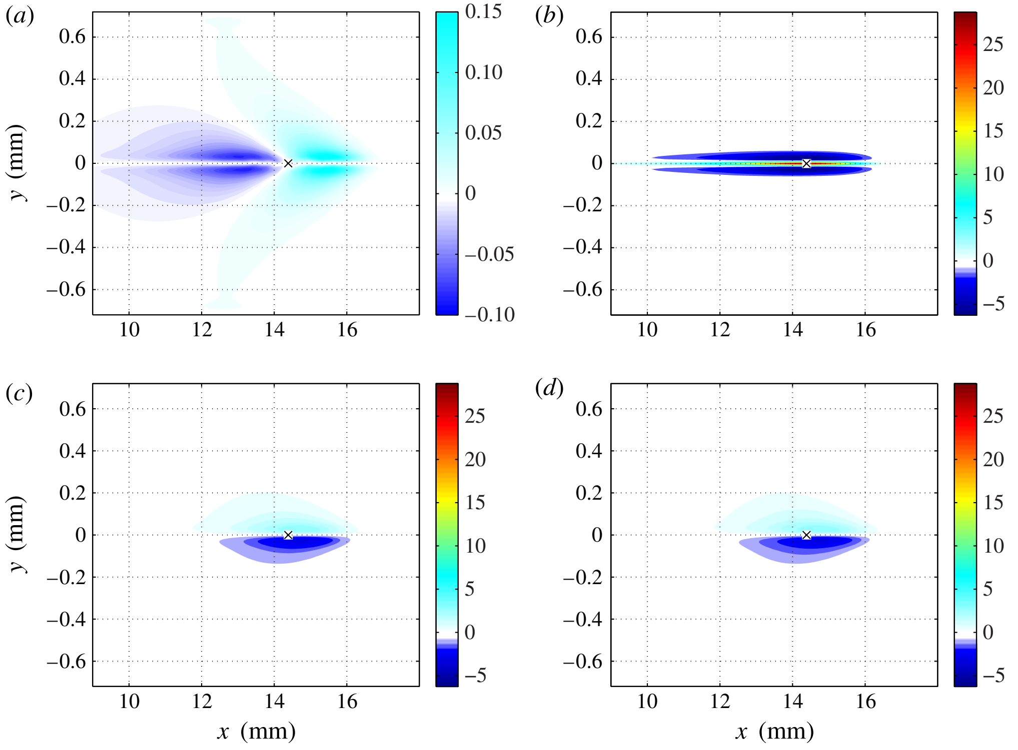

FIGURE 15. Components of the gradient of the Reynolds stress terms: (*a*) $-\rho\,\overline{u'\partial u'/\partial x}$; (*b*) $-\rho\,\overline{v'\partial u'/\partial y}$; (*c*) $-\rho\,\overline{u'\partial v'/\partial x}$; (*d*) $-\rho\,\overline{v'\partial v'/\partial y}$. They can be interpreted as force densities with units (N m^{-3}) which drive the Eulerian streaming motion in the modified model from § 4.2.2 (× indicates the location of the characteristic place).

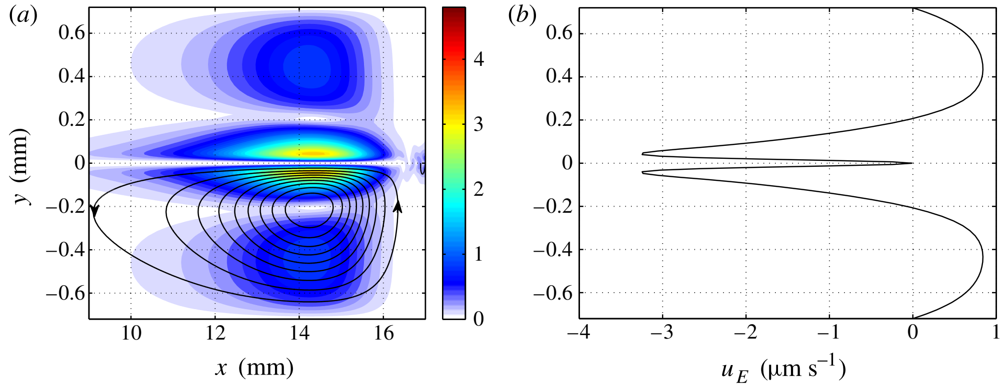

FIGURE 16. Eulerian mean velocity for the modified cochlear model (only Reynolds stresses; without streaming due to the moving BM): (*a*) streamlines with velocity magnitude (in µm s^{-1}); (*b*) axial velocity profile at the characteristic place. (The small wiggles in (*a*) at $x \approx 17$ mm are a numerical artefact due to the very slow convergence of the steady state.)

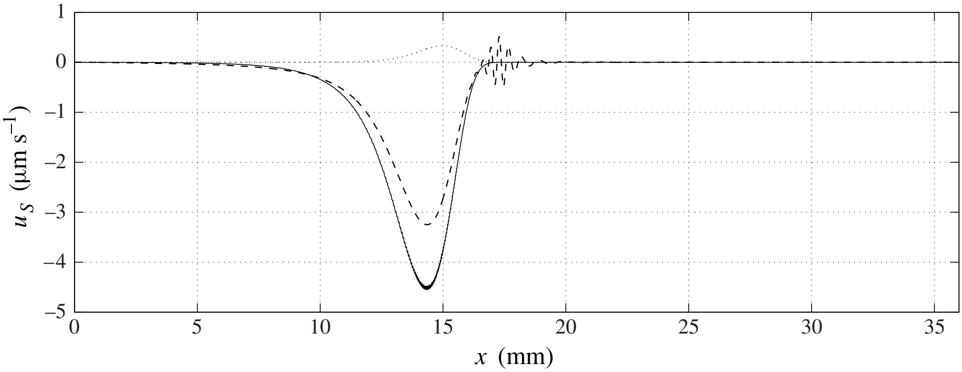

FIGURE 17. Eulerian slip velocities at the edge of the boundary layer: —— corrected slip velocity u_S (4.6); · · · · Lighthill's slip velocity u_S^L (4.2); – – – slip velocity obtained from the modified cochlear model (the small wiggles at $x \approx 17$ mm are a numerical artefact due to the very slow convergence of the steady state).

Figure 17 shows this corrected slip velocity u_S together the slip velocity obtained from the modified computational model. Although the agreement between u_S with the simulation results is not excellent, the corrected u_S is a much better prediction than u_S^L. The remaining differences between prediction and computational model can most likely be attributed to a transversal shifting of the velocity profiles (as we have studied in the previous section, cf. (4.4)) and to higher-order correction factors for u_S^L that are described in the appendix of Lighthill (1992).

4.2.3. *Summary of streaming sources*

We summarize our findings and list the relevant sources of streaming in the cochlea as follows: first, there is the Stokes drift represented by $\boldsymbol{u}_M$ (figures 7 and 11) which is well described by Lighthill's theoretical results; second, there is the streaming due to the moving BM which compensates for the Stokes drift at $y=0$ (figure 12); third, there is the streaming due to Reynolds stresses (figure 16). The latter two sources can be added because the streaming flow is governed by the linear Stokes equations. This superposition yields the Eulerian mean flow field $\boldsymbol{u}_E$ in figure 5. The vortices due to the moving BM and the vortices due to the Reynolds stresses nearly cancel each other in the bulk flow such that there remains only a pair of relatively weak vortices (rotating in counterclockwise direction above the BM).

Finally, the superposition of the Stokes drift and the Eulerian streaming yields the Lagrangian streaming field $\boldsymbol{u}_L = \boldsymbol{u}_M + \boldsymbol{u}_E$ (figure 6). It consists of a vortical flow in counterclockwise direction (above the BM) and a zero mean velocity on the BM.

4.3. *Magnitude of streaming velocities*

In order to assess the relevance of the cochlear streaming to physiological processes in the cochlea, it is necessary to estimate the magnitude of the streaming velocities for different stimulation frequencies and amplitudes. So far, we have only shown streaming flows that were obtained for a stimulation at 1000 Hz with $U_{in} = 30$ µm s^{-1} which corresponds to a sound pressure level of 76 dB in the ear canal (Sim *et al.* 2010).

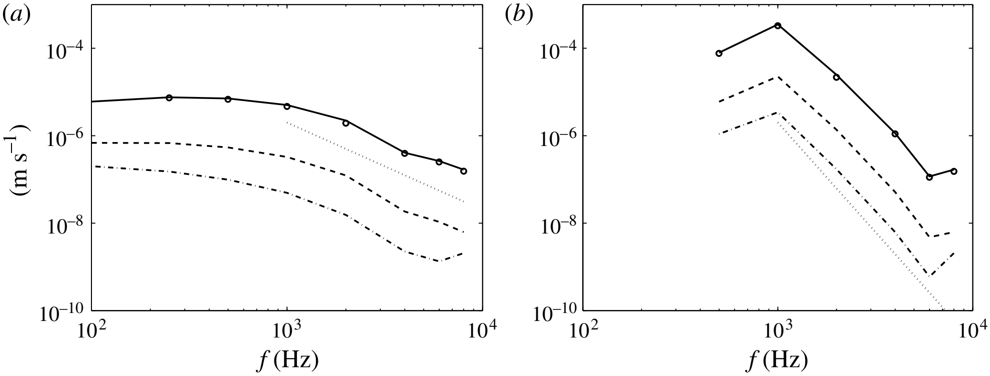

FIGURE 18. Maximum absolute values of the three terms of the corrected slip velocity (—— $\max_x |V^2/\sqrt{8\nu\omega}|$; – – – $\max_x |V^2k/4\omega|$; –·– $\max_x |3VV'/4\omega|$; cf. (4.6)) and maximum streaming velocities from the computational model (○ $\max_{x,y} |\boldsymbol{u_E}|$) for (*a*) $U_{in} = 30$ µm s^{-1} (corresponds to 76 dB SPL at 1000 Hz) and (*b*) a constant ear canal pressure amplitude of 94 dB (corresponding U_{in} taken from Sim *et al.* (2010)). The dotted lines indicate a decay rate of (*a*) $1/f^2$ and (*b*) $1/f^5$.

It is clear from expressions such as (4.5) that the streaming velocity scales with the square of the stapes velocity U_{in}. We have confirmed this quadratic scaling numerically by changing the stapes velocity amplitude to $U_{in} = 3$ µm s^{-1} and to 300 µm s^{-1}. The higher stapes velocity corresponds to a sound pressure level in the ear canal of approximately 96 dB. In this case, the maximum streaming velocities reach values of approximately 0.3 mm s^{-1} (which is still an order of magnitude below the primary wave velocities at the characteristic place).

The influence of the stimulation frequency on the streaming is less obvious from the theoretical results because the BM velocity amplitude V strongly depends on the frequency (cf. figure 3*b*) and because the terms in (4.6) scale either with $1/\omega$ or $1/\sqrt{\omega}$. Therefore, we have plotted in figure 18 the maximum absolute values of the three terms of the corrected slip velocity (4.6). To this end, we have extracted the amplitudes V and the wavenumbers k from simulations of the primary wave system for different stimulation frequencies. Figure 18 shows that higher stimulation frequencies yield, in general, smaller streaming velocities. The symbols in figure 18 indicate the streaming velocities obtained directly from the computational model. We find that the maximum Eulerian mean velocities are remarkably well predicted by $V^2/\sqrt{8\nu\omega}$ whereas the other terms in (4.6) play a minor role in the investigated frequency range. For a constant stapes velocity amplitude (figure 18*a*) streaming is strongest in a frequency range between 250 and 1000 Hz. For constant ear canal sound pressure levels (figure 18*b*) the highest streaming velocity of approximately 0.3 mm s^{-1} can be found at 1000 Hz. For higher frequencies f the maximum streaming velocity decays roughly like $1/f^2$ (for constant stapes velocity amplitude) and like $1/f^5$ (for constant sound pressure level). Therefore, we expect steady streaming to be most relevant for moderate to low-frequency hearing. This result stands in contrast to the common understanding that cochlear streaming is mainly a high-frequency phenomenon (Baker *et al.* 2006).

4.4. *Physiological relevance of cochlear streaming*

We have seen that cochlear streaming due to loud acoustical stimulations may reach values of the order of millimetres per second. In an actual human cochlea, the streaming velocities may be higher than the values found in our model. This is not so much due to the morphological differences (e.g. the tapering of the cochlea), but rather due to active cell processes which can considerably amplify the magnitude of the BM displacement. For soft tones this amplification reaches 40–60 dB (Hudspeth 2008). However, for higher sound intensity the active amplification is much smaller ('compressive nonlinearity', Hudspeth 2008). Apart from the amplification, the active processes lead to a sharper tuning of the cochlea, i.e. the peak at the characteristic place is narrower in an actual cochlea than the peaks shown in figure 3. This sharpening will mainly affect the second term in (4.6) because it scales with the gradient of the BM amplitude. From the available results (cf. figure 18) it is difficult to decide whether this effect is strong enough for the second term in (4.6) to become relevant for the streaming velocity.

Based on these arguments it appears that the streaming in the human cochlea might be sufficiently strong to support the deflection of the hair bundles of the inner hair cells at the characteristic place. Furthermore, it is reasonable to assume that a directed streaming flow would be more efficient in stimulating the inner hair cells than an oscillating flow which repeatedly opens and closes the ion channels while the acoustic stimulation lasts. This idea was originally formulated by Lighthill (1992) and briefly discussed by Baker *et al.* (2006). However, the results from the present work are not sufficient to prove or disprove Lighthill's idea of inner hair cell stimulation by streaming. Our simple box model is unable to appropriately represent the flow field in the vicinity of the inner hair cells because they are embedded in a complex three-dimensional structure (organ of Corti) with only a narrow gap giving access to the cochlear fluids (cf. figure 1*b*). It is likely that the streaming in this narrow gap is different from the streaming discussed here.

Apart from the inner hair cell stimulation, the streaming flow might be relevant for the transport of solutes in the lymphatic fluids of the cochlea. A convective transport of relevant metabolites (e.g. Na^+, K^+) might act in addition to the transport by molecular diffusion. This could enhance the re-establishment of concentration gradients which are necessary for the cell processes which generate the afferent nerve signals. Note that this enhancement of the transport capacity is adaptive in the sense that it acts where the nerve cells are active (i.e. at the characteristic place) and that its intensity increases with the sound intensity. Such an adaptive local advective transport mechanism reduces the need for blood vessels close to the organ of Corti which helps reducing the interference of mechanical noise of the blood flow with the hearing process. The Péclet number, $Pe = l \cdot u/D$, estimates the balance between the advective transport over a characteristic length scale l due to a streaming velocity u and the transport due to molecular diffusion characterized by the diffusion constant D. For $Pe > 1$ the advective transport is dominant. If we choose for the length scale l the distance from stria vascularis (highly vascularized region acting as a source of metabolites; cf. figure 1*b*) to the hair cells (consumer of metabolites), which is of the order of 10^{-4}–10^{-3} m, and if we further assume that the molecular diffusion coefficient in the lymphatic fluids is of the order of $10^{-9}\ \mathrm{m^2\ s^{-1}}$ (Cussler 2009), we find that advection due to streaming becomes the dominant transport process for streaming velocities higher than $10^{-5}\ \mathrm{m\ s^{-1}}$. Figure 18 suggests that such streaming velocities may be reached at moderately high sound intensities.

Finally, we would like to point out that streaming might also be useful for transporting drugs which are injected into the cochlea via e.g. the round window (Kingma, Miller & Myers 1992). Steady streaming might be used by applying targeted acoustic stimulations during specific time spans in order to use the maximum streaming velocities present at the characteristic place. Apart from the quasi-steady acoustic stimulations, such methods could also use specific non-harmonic acoustic stimulations which may possibly provide Lagrangian transport velocities that are significantly higher than the steady streaming velocities discussed here.

5. Concluding remarks

We have presented numerical results for steady streaming in a two-dimensional computational model of a passive cochlea. For moderate acoustic stimulations, the streaming velocities are of the order of micrometres per second. They can reach velocities of millimetres per second for loud sounds of 120 dB and more. The streaming is strongest in the vicinity of the characteristic place and forms a pair of counter-rotating vortices on either side of the BM. These results are in good qualitative agreement with the recent numerical study of Gerstenberger (2013).

In addition to the steady streaming flow, we found similar nonlinear phenomena related to the displacement of the BM. We described a small axial oscillation of the BM at twice the stimulation frequency such that the trajectory of a BM element has the shape of a figure of eight. We also found a steady axial displacement of the BM which results in an axial stretching of the BM in vicinity of the characteristic place.

Furthermore, we studied the different sources of streaming and found that the BM motion as well as the Reynolds stresses lead to a Eulerian mean flow. The Stokes drift has been predicted theoretically very well by Lighthill (1992), whereas his predictions for the Eulerian streaming require some modifications as he did not consider the streaming due to the moving BM. This effect leads to an Eulerian streaming flow even if the nonlinear advective terms of the Navier–Stokes equations are neglected.

The streaming due to the moving BM is also of relevance to numerical modelling. Oftentimes in computational fluid dynamics, small displacements of a vibrating wall are modelled by transpiration through a fixed wall, i.e. by a Dirichlet boundary condition for the wall-normal velocity while the wall itself remains in place. We have shown that this approximation leads to a correct primary flow field (e.g. a travelling wave) but that the resulting streaming flow is wrong. We observed this for the mean vortical flow above the BM which rotates in counterclockwise direction if the wall displacement is considered (figure 5) whereas it rotates clockwise if the wall displacement is neglected (figure 16). As we have confirmed in an independent numerical study, a similar phenomenon can be observed for the peristaltic transport in channels if the travelling wave on the wall has only small amplitudes. If the travelling wave is represented by an actual wall displacement, the net peristaltic transport is in the direction of the phase velocity of the travelling wave. If the wall displacement is modelled by wall transpiration only, the peristaltic transport goes in the opposite direction.

Finally, we tried to assess the relevance of steady streaming to the hearing process. We found that streaming is capable of supporting the local transport of metabolites to the organ of Corti. At the same time, we concluded that the results are not detailed enough to decide whether streaming plays a role in the stimulation of the inner hair cells. The strong decay of the streaming velocities for high frequencies (cf. figure 18) suggests that streaming should be mostly relevant to low-frequency hearing.

Acknowledgements

The work of E.E. was supported by ETH Research Grant ETH-17 09-2. Furthermore, we would like to thank T. Rösgen (ETH Zurich) for helpful discussions on steady streaming.

REFERENCES

ANDREWS, D. G. & MCINTYRE, M. E. 1978 An exact theory of nonlinear waves on a Lagrangian-mean flow. *J. Fluid Mech.* **89** (4), 609–646.

BAKER, G. J., ZETES-TOLOMEO, D. E., STEELE, C. R. & TOLOMEO, J. A. 2006 Cochlear mechanics. In *The Biomedical Engineering Handbook* (ed. J. P. Bronzino), chap. 63, CRC Press.

VON BÉKÉSY, G. 1960 *Experiments in Hearing*. McGraw-Hill.

BEYER, R. P. JR 1992 A computational model of the cochlea using the immersed boundary method. *J. Comput. Phys.* **98**, 145–162.

BÖHNKE, F. & SCHARFF, M. 2009 Acoustic streaming the cochlea. *SIAM J. Appl. Maths* **48**, 319–322.

BOLURIAAN, S. & MORRIS, P. J. 2003 Acoustic streaming: from Rayleigh to today. *Intl J. Aeroacoust.* **2** (3), 255–292.

BRADLEY, C. E. 1996 Acoustic streaming field structure: the influence of the radiator. *J. Acoust. Soc. Am.* **100** (3), 1399–1408.

BRADLEY, C. 2012 Acoustic streaming field structure. Part II. Examples that include boundary-driven flow. *J. Acoust. Soc. Am.* **131** (1), 13–23.

CUSSLER, E. L. 2009 *Diffusion: Mass Transfer in Fluid Systems*, 3rd edn, chap. 5, Cambridge University Press.

DE LA ROCHEFOUCAULD, O. & OLSON, E. S. 2007 The role of organ of Corti mass in passive cochlear tuning. *Biophys. J.* **93**, 3434–3450.

DING, X., LI, P., LIN, S.-C. S., STRATTON, Z. S., NAMA, N., GUO, F., SLOTCAVAGE, D., MAO, X., SHI, J., COSTANZO, F. & HUANG, T. J. 2013 Surface acoustic wave microfluidics. *Lab on a Chip* **13**, 3226–3649.

EDOM, E., OBRIST, D., HENNIGER, R., SIM, J.-H., HUBER, A. H. & KLEISER, L. 2013 The effect of rocking stapes motions on the cochlear fluid flow and on the basilar membrane motion. *J. Acoust. Soc. Am.* **134** (5), 3749–3758.

EMADI, G., RICHTER, C.-P. & DALLOS, P. 2004 Stiffness of the gerbil basilar membrane: radial and longitudinal variations. *J. Neurophysiol.* **91** (1), 474–488.

GERSTENBERGER, C. 2013 Numerical simulation of acoustic streaming within the cochlea. PhD thesis, Leibniz Universität Hannover.

GERSTENBERGER, C. & WOLTERS, F.-E. 2011 Numerical simulation of acoustic streaming within a biological fluid–structure coupled system like the cochlea. In *Fortschritte der Akustik – DAGA 2011* (ed. J. Becker-Schweitzer & G. Notbohm), vol. 2, pp. 817–818. Deutsche Gesellschaft für Akustik e.V. (DEGA).

GIVELBERG, E. & BUNN, J. 2003 A comprehensive three-dimensional model of the cochlea. *J. Comput. Phys.* **191**, 377–391.

HENNIGER, R., OBRIST, D. & KLEISER, L. 2010 High-order accurate solution of the incompressible Navier–Stokes equations on massively parallel computers. *J. Comput. Phys.* **229**, 3543–3572.

HILL, D. C. 1995 Adjoint systems and their role in the receptivity problem for boundary layers. *J. Fluid Mech.* **292**, 183–204.

HUANG, N. E., SHEN, Z., LONG, S. R., WU, M. C., SHIH, H. H., ZHENG, Q., YEN, N.-C., TUNG, C. C. & LIU, H. H. 1998 The empirical mode decomposition and the Hilbert spectrum for nonlinear and non-stationary time series analysis. *Proc. R. Soc.* A **454** (1971), 903–995.

HUDSPETH, A. J. 2008 Making an effort to listen: mechanical amplification in the ear. *Neuron* **59** (4), 530–545.

KINGMA, G. G., MILLER, J. M. & MYERS, M. W. 1992 Chronic drug infusion into the scala tympani of the guinea pig cochlea. *J. Neurosci. Methods* **45**, 127–134.

KOTAS, C. W., ROGERS, P. H. & YODA, M. 2011 Acoustically induced streaming flows near a model cod otolith and their potential implications for fish hearing. *J. Acoust. Soc. Am.* **130** (2), 1049–1059.

LESSER, M. B. & BERKLEY, D. A. 1972 Fluid mechanics of the cochlea. Part 1. *J. Fluid Mech.* **51** (3), 497–512.

LIGHTHILL, J. 1978 Acoustic streaming. *J. Sound Vib.* **61**, 391–418.

LIGHTHILL, J. 1981 Energy flow in the cochlea. *J. Fluid Mech.* **106**, 149–213.

LIGHTHILL, J. 1992 Acoustic streaming in the ear itself. *J. Fluid Mech.* **239**, 551–606.

LUCHINI, P. & CHARRU, F. 2005 Acoustic streaming past a vibrating wall. *Phys. Fluids* **17** (12), 122106.

NAIDU, R. C. & MOUNTAIN, D. C. 2001 Longitudinal coupling in the basilar membrane. *J. Assoc. Res. Oto.* **2**, 257–267.

PESKIN, C. S. 2002 The immersed boundary method. *Acta Numerica* **11**, 479–517.

PETERSON, L. C. & BOGERT, B. P. 1950 A dynamical theory of the cochlea. *J. Acoust. Soc. Am.* **22** (3), 369–381.

POZRIKIDIS, C. 2008 Boundary-integral modeling of cochlear hydrodynamics. *J. Fluids Struct.* **24**, 336–365.

RILEY, N. 2001 Steady streaming. *Annu. Rev. Fluid Mech.* **33**, 43–65.

SIM, J. H., CHATZIMICHALIS, M., LAUXMANN, M., RÖÖSLI, C., EIBER, A. & HUBER, A. M. 2010 Complex stapes motions in human ears. *J. Assoc. Res. Oto.* **11**, 329–341.

SUH, Y. K. & KANG, S. 2008 Acoustic streaming. In *Encyclopedia of Microfluidics and Nanofluidics* (ed. D. Li), Springer.

TAN, M. K., FRIEND, J. R., MATAR, O. K. & YEO, L. Y. 2010 Capillary wave motion excited by high frequency surface acoustic waves. *Phys. Fluids* **22** (11), 112112.

VANNESTE, J. & BÜHLER, O. 2011 Streaming by leaky surface acoustic waves. *Proc. R. Soc.* A **467** (2130), 1779–1800.

WITTBRODT, M. J., STEELE, C. R. & PURIA, S. 2006 Developing a physical model of the human cochlea using microfabrication methods. *Audiol. Neuro-Otol.* **11**, 104–112.